# Bayesian sparse regularization for parallel MRI reconstruction using Complex Bernoulli-Laplace mixture priors

Siwar Chaabene, Lotfi Chaari, Abdelaziz Kallel

# Bayesian sparse regularization for parallel MRI reconstruction using Complex Bernoulli-Laplace mixture priors

**Siwar Chaabene**[1,2] · **Lotfi Chaari**[3] · **Abdelaziz Kallel**[2]

**Abstract** Parallel imaging technique using several receiver coils provides a fast acquisition of Magnetic Resonance Imaging (MRI) images with high temporal and/or spatial resolutions. Against this background, the most difficult task is the full Field of View (FoV) images reconstruction without noise, distortions and artifacts. In this context, SENSitivity Encoding (SENSE) is considered the most often used parallel Magnetic Resonance Imaging (pMRI) reconstruction method in the clinical application. On one side, solving the inherent reconstruction problems has known significant progress during the last decade. On other side, the sparse Bayesian regularization for signal/image recovery has generated a great research interest especially when large volumes of data are processed. The purpose of this paper is to develop a novel Bayesian regularization technique for sparse pMRI reconstruction. The new technique is based on a Hierarchical Bayesian Model (HBM) using a complex Bernoulli-Laplace mixture in order to promote two sparsity levels for the target image. The inference is conducted using a Markov chain Monte Carlo (MCMC) sampling scheme. Simulation results obtained with both synthetic and real datasets are showing the outperformance of the proposed sparse Bayesian technique compared to other existing regularization techniques.

**Keywords** Sparse Bayesian model · $\ell_0 + \ell_1$ regularization · MCMC · Gibbs sampler · parallel MRI restoration · SENSE

S. Chaabene
siwarchaabene@gmail.com

L. Chaari
lotfi.chaari@toulouse-inp.fr

A. Kallel
abdelaziz.kallel@crns.rnrt.tn

[1] Multimedia InfoRmation systems and Advanced Computing Laboratory (MIRACL), University of Sfax, 3021 Sfax, Tunisia.
[2] Digital Research Center of Sfax, B.P. 275, Sakiet Ezzit, 3021 Sfax, Tunisia.
[3] University of Toulouse, IRIT-ENSEEIHT (UMR 5505), Toulouse, France.

## 1 Introduction

Magnetic Resonance Imaging (MRI) is a powerful imaging technique that enables producing accurate images in order to visualize with great precision many organs of the human body. In fact, classical MRI uses a single receiver coil to capture the MRI data acquisition in the Fourier space (i.e., the k-space). However, the major drawback of MRI is its time-consuming acquisition to capture all the data needed to rebuild a full Field of View (FoV) image. For this reason, MRI images with fast data acquisition, high spatial and temporal resolutions, and without artifacts represent a great interest for researchers in various research activities, like functional MRI where several data volumes have to be acquired during the application of an experimental paradigm to stimulate patients. This goal can be achieved using parallel Magnetic Resonance Imaging (pMRI) [1] with several receiver coils using different spatial sensitivity profiles. This helps to reduce the exposure time of the patient to the MRI environment, to accelerate the acquisition of MRI data, and to improve spatial and/or temporal resolutions of the images. Following the parallel imaging principle, each receiver coil acquires in the k-space a sub-sampled data using a reduction (sub-sampling) factor $R$. This k-space sub-sampling consists of acquiring one line over $R$ usu-

ally along the phase encoding direction, which generally leads to a sampling below the Nyquist rate [2]. The measured reduced FoV images present aliasing artifacts in the image domain after an inverse Fourier transform. Therefore, the pMRI reconstruction technique consists of combining reduced FoV images of multiple receiver coils in order to reconstruct the full FoV image. Accordingly, this reconstruction procedure may be performed by three types of algorithms: *i)* reconstruction in the spatial domain (SENSitivity Encoding (SENSE) [1]), *ii)* reconstruction in the k-space (Generalized Autocalibrating Partially Parallel Acquisitions (GRAPPA) [3]) and *iii)* hybrid algorithms combining the two reconstructions (Sensitivity Profiles from an Array of Coils for Encoding and Reconstruction In Parallel (SPACE RIP) [4]). A comparative study in [5] shows that the SENSE technique is the most often used in the clinical routine application. Compressed sensing [6] also makes it possible to accelerate the data acquisition [7–11]. In this paper, we concentrate on the SENSE method as operating in the original space. In practice, the pMRI reconstruction problem do not meet the expectations presented by the Hadamard conditions [12] due to severe acquisition conditions under high reduction factors. Therefore, the inverse pMRI reconstruction problem based on the SENSE method is often ill-posed [13]. On one side, the works addressed in [13–17] have been suggested to regularize this ill-posed problem during the past years. More recently, other techniques [18,19] have been proposed to account for potential sensitivity errors during the reconstruction process. On other side, several works in the recent Bayesian literature [20–23] have been proposed using the $\ell_0 + \ell_1$ regularization effect for sparse image recovery. The use of this effect has demonstrated its ability to provide flexible and adaptive regularizations for the resolution of ill-posed inverse problems. Generally, the use of a Bernoulli and continuous distributions mixture priors like multivariate Bernoulli-Laplace [24,25], Bernoulli-Gaussian [26], Bernoulli-Exponential [20] and Bernoulli-generalized Gaussian-Laplace [27] allows promoting the desired image sparsity levels directly in the original space. These Bayesian Bernoulli-based models enable to estimate the regularization parameters and hyperparameters directly from the observed data, which is not possible with other variational methods [6, 13, 17, 28]. The estimation of these parameters and hyperparameters is performed using Monte Carlo Markov chains (MCMC) [29] sampling techniques. These latter are used to simulate samples from the target distributions and to obtain accurate estimates afterwards. For this reason, we resort here to a Bayesian framework in order to develop a fully automatic regularization method for pMRI reconstruction. This will allow us to avoid needing a reference scan to estimate the regularization parameters, which is generally essential for variational regularization techniques. In this paper, we propose a new Bayesian regularization technique for sparse parallel MRI based on a $\ell_0 + \ell_1$ regularization to estimate a complex-valued target image. This prior promotes directly in the original space two sparsity levels of the desired image without using any transform. It is worth noting that we use here the same model as in [30]. In this paper, a more detailed presentation of the whole model is given. We also provide more validations especially by adding experiments on real data that illustrate our reconstruction method performance under real and severe experimental conditions. These validations have been conducted with data acquired at both 1.5 and 3 Tesla magnetic fields. The paper is structured as follows. In Section 2, we introduce the problem statement of the pMRI restoration. Section 3 presents the proposed Hierarchical Bayesian model (HBM). Section 4 shows the resolution scheme for this model. In Section 5, we validate our sparse model on complex-valued synthetic and real pMRI data. Finally, conclusions with some future work are described in Section 6.

## 2 Problem Statement

The pMRI observation model [1, 17] in the spatial domain at each position $\boldsymbol{x}$ writes

$$\boldsymbol{d}(\boldsymbol{x}) = \boldsymbol{S}(\boldsymbol{x})\boldsymbol{\rho}(\boldsymbol{x}) + \boldsymbol{n}(\boldsymbol{x}), \tag{1}$$

where $\boldsymbol{d}$ is the complex-valued observed signal, $\boldsymbol{S}$ is the sensitivity maps operator, $\boldsymbol{\rho}$ represents the target image, while $\boldsymbol{n}$ stands for the observation noise. The matrix $\boldsymbol{S}$ is generally ill-conditioned and the pMRI reconstruction problem is ill-posed. Our objective is to estimate $\boldsymbol{\rho}$ from $\boldsymbol{d}$ and the knowledge about $\boldsymbol{S}$. Solving this problem following the SENSE procedure resorts to a maximum likelihood estimation (MLE). At each spatial position $\boldsymbol{x}$, the estimate writes as

$$\hat{\boldsymbol{\rho}}_{\text{MLE}}(\boldsymbol{x}) = \left(\boldsymbol{S}^H(\boldsymbol{x})\Psi^{-1}\boldsymbol{S}(\boldsymbol{x})\right)^{\sharp}\boldsymbol{S}^H(\boldsymbol{x})\Psi^{-1}\boldsymbol{d}(\boldsymbol{x}), \tag{2}$$

where $\Psi^{-1}$ represent the noise covariance matrix which is generally pre-estimated by a reference acquisition, $(.)^H$ denotes the transposed complex conjugate and $(.)^{\sharp}$ denotes the pseudo-inverse. As already reported in a number of studies of the literature [17, 28], SENSE reconstruction provides images that generally suffer from several imperfections especially when the acquisition conditions are poor (high reduction factor, high noise level,...). Regularization is therefore essential to cope with this problem and provide accurate reconstruction

of images. Several variational methods have therefore been proposed in the literature using either wavelet transforms [17] or total variation (TV) regularization [15]. These methods provide better images than the SENSE method, but request setting regularization parameters that have to be *a priori* estimated. This prior estimation can be performed based on a reference scan, which is not always possible. For this reason, we resort in this paper to a Bayesian framework where we design a fully automatic regularization method that directly calculates the regularization parameters and hyperparameters from the observed data along with the target images.

## 3 Hierarchical Bayesian model

In the present section, we detail our HBM designed to perform automatic regularized reconstruction of pMRI images. Following a probabilistic approach, all the model parameters and hyperparameters are supposed to be realizations of random variables. Moreover, we account in our model construction for the complex-valued nature of pMRI data.

### 3.1 Likelihood

Assuming that $\boldsymbol{n}$ is Complex additive Gaussian noise with $\Psi = \sigma_n^2 I$, where $I$ represents the identity matrix, the likelihood with the linear model in (1) can be defined as

$$f(\boldsymbol{d}|\boldsymbol{\rho}, \sigma_n^2) = \frac{\prod_{\boldsymbol{x}} \exp\left(-\|\boldsymbol{d}(\boldsymbol{x}) - \boldsymbol{S}(\boldsymbol{x})\boldsymbol{\rho}(\boldsymbol{x})\|^2_{\Psi^{-1}}\right)}{(2\pi)^{Q/2}|\Psi|^{1/2}}, \quad (3)$$

where $Q$ is the number of coefficients in the observed data.

### 3.2 Priors

In this subsection, we assign prior distributions to the unknown parameter vector $\boldsymbol{\theta} = \left\{\boldsymbol{\rho}, \sigma_n^2\right\}$.

#### *3.2.1 Prior distribution for $\boldsymbol{\rho}$*

A Bernoulli-Laplace (BL) mixture prior is assigned to $\boldsymbol{\rho}$. This BL prior allows to promote two sparsity levels of the target image in the original space. The first one serves to capture coefficients that exactly equal to zero, whereas the second one promotes sparsity within the non-zero coefficients. Note that the BL prior is affected to complex-valued data. In this case, we assume that the real and imaginary parts are used separately and independently. Supposing that every complex coefficient $\rho_i (i = 1, ..., K)$ can be defined as

$$\rho_i = y_i + j z_i, \quad (4)$$

where $j^2 = -1$, $y_i$ (resp. $z_i$) denotes the real (resp. imaginary) part of the complex desired image $\rho_i$, and $K$ represents the number of coefficients of $\boldsymbol{\rho}$).
Assuming that $y_i$ and $z_i$ are independent, the BL prior can be written as follows

$$\begin{aligned} f(\rho_i|\omega, \lambda) &= f(y_i|\omega, \lambda) f(z_i|\omega, \lambda) \\ &= \left[(1-\omega)\,\delta(y_i) + \omega \frac{1}{2\lambda} \exp\left(-\frac{|y_i|}{\lambda}\right)\right] \\ &\times \left[(1-\omega)\,\delta(z_i) + \omega \frac{1}{2\lambda} \exp\left(-\frac{|z_i|}{\lambda}\right)\right], \end{aligned} \quad (5)$$

where $\omega$ represents a weight belonging to $[0, 1]$, $\lambda$ assesses the non-zero coefficients sparsity level of $y_i$ and $z_i$ parts, and $\delta(.)$ represents the Dirac delta function. It should be noted that various hyperparameters could be considered for each part.
Supposing independence between the complex coefficients $\rho_i$, the BL distribution of the desired image $\boldsymbol{\rho}$ writes

$$f(\boldsymbol{\rho}|\omega, \lambda) = \prod_{i=1}^{K} f(\rho_i|\omega, \lambda). \quad (6)$$

#### *3.2.2 Prior distribution for $\sigma_n^2$*

The positivity of the noise variance $\sigma_n^2$ can be guaranteed when an inverse-Gamma (IG) prior with two hyperparameters $\gamma$ and $\varepsilon$ is adopted

$$\begin{aligned} f(\sigma_n^2|\gamma, \varepsilon) &= \mathcal{IG}(\sigma_n^2|\gamma, \varepsilon) \\ &= \frac{\varepsilon^\gamma}{\Gamma(\gamma)} \left(\sigma_n^2\right)^{-1-\gamma} \exp\left(-\frac{\varepsilon}{\sigma_n^2}\right), \end{aligned} \quad (7)$$

where $\Gamma(.)$ denoted the standard gamma function. The shape and scale hyperparameters $\gamma$ and $\varepsilon$ have been set to $10^{-1}$ to keep a non-informative prior.

### 3.3 Hyperparameter priors

In this subsection, we define the choice of the hyperprior distributions affected for the unknown hyperparameter vector denoted by $\boldsymbol{\Phi} = \{\omega, \lambda\}$.

#### *3.3.1 Hyperprior distribution for $\omega$*

A uniform prior on $[0, 1]$ is assigned for the weight $\omega$, i.e., $\mathcal{U}_{[0,1]}(\omega)$. The weight $\omega$ indicates the non-zero coefficients rate in the desired image.

#### *3.3.2 Hyperprior distribution for $\lambda$*

A IG prior is used for $\lambda$ that guarantees the positivity of this defined as

$$f(\lambda|\nu, \alpha) = \mathcal{IG}(\lambda|\nu, \alpha) = \frac{\alpha^\nu}{\Gamma(\nu)} \lambda^{-1-\nu} \exp\left(-\frac{\alpha}{\lambda}\right). \quad (8)$$

where the hyperparameters $\nu$ and $\alpha$ are fixed to $10^{-1}$ in order to keep a non-informative prior.
In summary, the directed acyclic graph (DAG) of our HBM is represented in Fig. 1 where the unknown parameters and hyperparameters appear in circles and the fixed hyperparameters appear into squares.

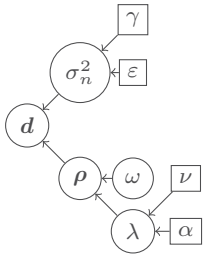


Fig. 1: DAG of our HBM.

The next section explains the Bayesian inference scheme with the sampling techniques used to construct a correct Bayesian estimators for the unknown parameter vector $\{\boldsymbol{\theta}, \boldsymbol{\Phi}\}$.

## 4 Bayesian Inference Scheme

Taking into account the HBM introduced in the previous section, we use a maximum a posterior (MAP) estimation for the unknown model parameters and hyperparameters. By the Bayes' paradigm, the joint posterior of the parameter/hyperparameter vector $\{\boldsymbol{\theta}, \boldsymbol{\Phi}\}$ can be represented as

$$\begin{aligned} f\left(\boldsymbol{\theta}, \boldsymbol{\Phi} | \boldsymbol{d}\right) &\propto f\left(\boldsymbol{d} | \boldsymbol{\theta}\right) f\left(\boldsymbol{\theta} | \boldsymbol{\Phi}\right) f\left(\boldsymbol{\Phi} | \gamma, \varepsilon, \nu, \alpha\right) \qquad (9) \\ &\propto f(\boldsymbol{d} | \boldsymbol{\rho}, \sigma_n^2) f(\boldsymbol{\rho} | \omega, \lambda) f(\sigma_n^2 | \gamma, \varepsilon) f(\omega) f(\lambda | \nu, \alpha). \end{aligned}$$

The corresponding joint posterior distribution of the proposed sparse Bayesian model based on the distributions adopted in Section 3 takes the following formula

$$\begin{aligned} f\left(\boldsymbol{\theta}, \boldsymbol{\Phi} | \boldsymbol{d}\right) \propto & \frac{\prod\limits_{\boldsymbol{x}} \exp\left(-\left\|\boldsymbol{d}(\boldsymbol{x}) - \boldsymbol{S}(\boldsymbol{x})\boldsymbol{\rho}(\boldsymbol{x})\right\|_{\Psi^{-1}}^2\right)}{(2\pi)^{Q/2}|\Psi|^{1/2}} \\ & \times \prod_{i=1}^{K} \left[ \left( (1-\omega)\delta(y_i) + \omega \frac{1}{2\lambda} \exp(-\frac{|y_i|}{\lambda}) \right) \right. \\ & \left. \times \left( (1-\omega)\delta(z_i) + \omega \frac{1}{2\lambda} \exp(-\frac{|z_i|}{\lambda}) \right) \right] \\ & \times \mathcal{U}\left(\omega\right) \times \frac{\alpha^{\nu}}{\Gamma(\nu)} \left(\lambda\right)^{-1-\nu} \exp\left(-\frac{\alpha}{\lambda}\right) 1_{\mathbb{R}^+}(\lambda). \end{aligned} \qquad (10)$$

The complicated distribution in (10) does not allow us to derive closed-form expressions for the Bayesian estimators of $\{\boldsymbol{\theta}, \boldsymbol{\Phi}\}$. As a consequence, we propose to use the MCMC method for sample this joint posterior distribution. More precisely, we use here a Gibbs sampler (GS) algorithm that iteratively draws in samples of the unknown parameters and hyperparameters according to the conditional posterior distributions $f(\boldsymbol{\rho}|\boldsymbol{d}, \sigma_n^2, \omega, \lambda)$, $f(\omega|\boldsymbol{\rho})$, $f(\lambda|\boldsymbol{\rho}, \nu, \alpha)$ and $f(\sigma_n^2|\boldsymbol{d}, \boldsymbol{\rho}, \gamma, \varepsilon)$.

### 4.1 Conditional posterior distribution of $\sigma_n^2$

The combination of the likelihood in (3) and the prior of $\sigma_n^2$ in (7) gives the following IG distribution

$$\sigma_n^2 | \boldsymbol{d}, \boldsymbol{\rho}, \gamma, \varepsilon \sim IG\left(\gamma + \frac{Q}{2}, \varepsilon + \frac{\|\boldsymbol{d} - \boldsymbol{S}\boldsymbol{\rho}\|_2^2}{2}\right), \qquad (11)$$

where $\|.\|_2$ refer to the Euclidean norm. The distribution in (11) can be easily sampled.

### 4.2 Conditional posterior distribution of $\lambda$

Similar to [20], the combination of (6) and (8) leads to the following conditional posterior distribution

$$\lambda | \boldsymbol{\rho}, \nu, \alpha \sim IG\left(\nu + \|\boldsymbol{\rho}\|_0, \alpha + \|\boldsymbol{\rho}\|_1\right). \qquad (12)$$

where $\|.\|_0$ denotes $\ell_0$ the pseudo-norm and $\|.\|_1$ signify $\ell_1$ norm. The distribution in (12) can be easily sampled.

### 4.3 Conditional posterior distribution of $\omega$

Calculations similar to [21] show that $\omega$ follows a Beta distribution

$$\omega | \boldsymbol{\rho} \sim B\left(1 + \|\boldsymbol{\rho}\|_0, 1 + Q - \|\boldsymbol{\rho}\|_0\right). \qquad (13)$$

The distribution in (13) can be easily sampled.

### 4.4 Conditional posterior distribution of $\boldsymbol{\rho}$

It is worth noting that $y_i$ and $z_i$ are independent. Their conditional posterior distributions can be expressed respectively by

$$\begin{aligned} f(y_i | \boldsymbol{d}, \tilde{\boldsymbol{\rho}}_i, \sigma_n^2, \omega, \lambda) = & \omega_{1,i}^y \delta(y_i) + \omega_{2,i}^y \mathcal{N}^+ \ \ \mu_{y,i}^+, \sigma_i^2) \\ & + \omega_{3,i}^y \mathcal{N}^- \ \ \mu_{y,i}^-, \sigma_i^2), \end{aligned} \qquad (14)$$

and

$$\begin{aligned} f(z_i | \boldsymbol{d}, \tilde{\boldsymbol{\rho}}_i, \sigma_n^2, \omega, \lambda) = & \omega_{1,i}^z \delta(z_i) + \omega_{2,i}^z \mathcal{N}^+ \ \ \mu_{z,i}^+, \sigma_i^2) \\ & + \omega_{3,i}^z \mathcal{N}^- \ \ \mu_{z,i}^-, \sigma_i^2), \end{aligned} \qquad (15)$$

where $\mathcal{N}^+$ and $\mathcal{N}^-$ represent the truncated Gaussian distributions on $\mathbb{R}^+$ and $\mathbb{R}^-$, respectively.

The desired image $\boldsymbol{\rho}$ decomposes onto the orthonormal basis $B = \{e_1, ..., e_K\}$ such that $\boldsymbol{\rho} = \tilde{\boldsymbol{\rho}}_i + \rho_i \boldsymbol{e}_i$ where $\tilde{\boldsymbol{\rho}}_i$ is obtained by setting the $i^{th}$ element of $\boldsymbol{\rho}$ to 0 denoted as $\boldsymbol{v}_i = \boldsymbol{d} - \boldsymbol{S}\tilde{\boldsymbol{\rho}}_i$ and $\boldsymbol{s}_i = \boldsymbol{S}\boldsymbol{e}_i$.

The weights $\left(\omega_{l,i}^y\right)_{1 \leq l \leq 3}$ used in (14) are defined as

$$\omega_{l,i}^y = \frac{u_{l,i}^y}{\sum\limits_{l=1}^{3} u_{l,i}^y} \qquad (16)$$

where

$u_{1,i}^y = 1 - \omega$,

$u_{2,i}^y = \frac{\omega}{4\lambda^2} \exp\left(\frac{\left(\mu_{y,i}^+\right)^2}{2\sigma_i^2}\right) \sqrt{2\pi\sigma_i^2} G \ \ \mu_{y,i}^+, \sigma_i^2)$,

$u_{3,i}^y = \frac{\omega}{4\lambda^2} \exp\left(\frac{\left(\mu_{y,i}^-\right)^2}{2\sigma_i^2}\right) \sqrt{2\pi\sigma_i^2} G \ \ -\mu_{y,i}^-, \sigma_i^2)$,

and

$$\begin{aligned} \sigma_i^2 &= \frac{\sigma_n^2}{\|\boldsymbol{s}_i\|_2^2}, \\ \mu_{y,i}^+ &= \sigma_i^2 \left(\frac{Real\left(\boldsymbol{v}_i^T \boldsymbol{s}_i\right)}{\sigma_n^2} - \frac{1}{\lambda}\right), \\ \mu_{y,i}^- &= \sigma_i^2 \left(\frac{Real\left(\boldsymbol{v}_i^T \boldsymbol{s}_i\right)}{\sigma_n^2} + \frac{1}{\lambda}\right), \\ G \ \ \mu, \sigma^2) &= \sqrt{\frac{\sigma^2\pi}{2}} \left(1 + erf\left(\frac{\mu}{\sqrt{2\sigma^2}}\right)\right). \end{aligned}$$

The weights $\left(\omega_{l,i}^{z}\right)_{1\leq l\leq 3}$ used in (15) have the same expressions for the weights $\left(\omega_{l,i}^{y}\right)_{1\leq l\leq 3}$.
Algorithm 1 summarizes the main steps of the designed GS for pMRI reconstruction. The GS algorithm consists of generating samples distributed for these unknown parameters and hyperparameters according to their conditional posterior distributions. In our experiments, the GS algorithm is executed 60 runs with 30 iterations as the burn-in period to reach convergence. It is worth noting that the burn-in period has been empirically set since it is not possible to a prior estimated it. Resorting to convergence monitoring techniques [31] will also dramatically increase the algorithm complexity.

**Algorithm 1:** GS.

Initialize $\boldsymbol{\rho}^{(\mathbf{0})}$ ;
**repeat**
  Sample $\sigma_n^2$ according to $f(\sigma_n^2|\boldsymbol{d},\boldsymbol{\rho},\gamma,\varepsilon)$.
  Sample $\lambda$ according to $f(\lambda|\boldsymbol{\rho},\nu,\alpha)$.
  Sample $\omega$ according to $f(\omega|\boldsymbol{\rho})$.
  **for** $i = 1 \dots K$ **do**
    Sample $y_i$ according to $f(y_i|\boldsymbol{d},\tilde{\boldsymbol{\rho}}_i,\sigma_n^2,\omega,\lambda)$.
    Sample $z_i$ according to $f(z_i|\boldsymbol{d},\tilde{\boldsymbol{\rho}}_i,\sigma_n^2,\omega,\lambda)$.
  **end**
**until** *convergence*;

Based on the chains sampled by our algorithm, and after discarding the samples corresponding to the burn-in period, we estimate the target image $\hat{\boldsymbol{\rho}}$ using a MAP estimator in order to let the Bernoulli prior express the sparsity level of the estimates. For $\hat{\sigma_n^2}$ and the hyperparameters $\hat{\omega}$ and $\hat{\lambda}$, a minimum mean square error (MMSE) estimator has been used as commonly done in the literature. The flowchart of the proposed framework is represented in Fig. 2.

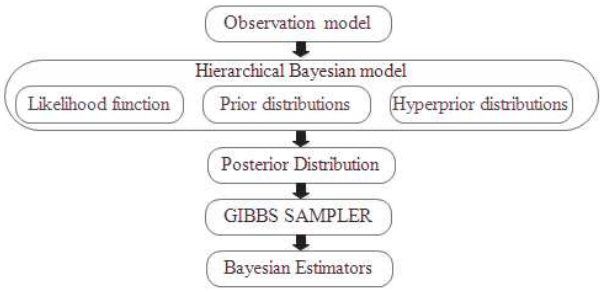


Fig. 2: The flowchart of the proposed framework.

## 5 Experimental Validation

The proposed sparse Bayesian model presented in the previous two sections was tested and validated on both complex-valued synthetic and real pMRI data. Our implementation has been performed using Matlab R2016a on a laptop with i7-7500U Intel core processor (3.5GHz, RAM 8GB) which corresponds to about 11 minutes of computational time. Synthetic data experiment was conducted to appraise the robustness of our algorithm with respect to the known reference image. However, real data experiments were conducted to illustrate the reconstruction performance on real pMRI data since no ground truth is available in this case.

### 5.1 Experiment with Synthetic data

To prove the effectiveness of our model, an experiment was performed on a synthetic complex-valued pMRI dataset. The reference image of size $256 \times 256$ is shown in Fig. 3(a). The observations have been simulated with severe acquisition conditions using a high reduction factor $R = 4$, $L = 8$ receiver coils and uncertainties in the sensitivity maps using a Gaussian white noise of variance equal to 0.001. The pMRI data have been simulated by a complex Gaussian noise of variance $\sigma_n^2 = 5$. Figs. 3(b) and 3(c) display the restored images by the SENSE method and the proposed sparse Bayesian model, respectively. To compare with methods of the literature, reconstructed slices are obtained by two recent regularizations techniques such as the Bayesian $\ell_2$ [18] and the Tikhonov [32]. Figs. 3(d) and 3(e) illustrate the restored images.

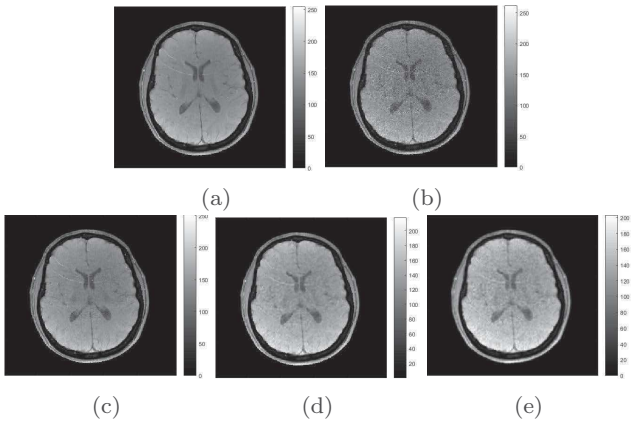


Fig. 3: (a) Ground truth, Restored image by : (b) the SENSE method, (c) the proposed sparse model, (d) the Bayesian $\ell_2$ regularization, and (e) the Tikhonov regularization.

The Tikhonov regularization can be defined as

$$\min_{\boldsymbol{\rho}(\boldsymbol{x})} \left\{ \|\boldsymbol{d}(\boldsymbol{x}) - \boldsymbol{S}(\boldsymbol{x})\boldsymbol{\rho}(\boldsymbol{x})\|^2_{\boldsymbol{\Psi}^{-1}} + \iota \|\boldsymbol{\rho}(\boldsymbol{x}) - \boldsymbol{\rho_{GT}}(\boldsymbol{x})\|^2 \right\} \quad (17)$$

where $\iota \geq 0$ is the regularization which is difficult to set automatically and $\boldsymbol{\rho_{GT}}$ represent the ground truth image. This regularization is fast and easy to implement. However, oversmoothing generally occur as illustrated in Fig. 3(e). As regards the the Bayesian $\ell_2$ regularization method and the proposed model, they more time-consuming. However, these methods have the advantages to give more flexibility to the level of the information a prior used, and to be more automatic since all

the model parameters/ hyperparameters are directly estimated from the observed data. Visually, the proposed model allows to reduce reconstruction artifacts without introducing any oversmoothing aspect and offers a less noisy reconstruction in contrast to Bayesian $\ell_2$ and Tikhonov regularizations. In addition, it is evident that our sparse model helps to restore slice with lower smoothing levels than other methods. For the sake of quantitative assessment of the image quality [33], Tab.1 indicates the structural similarity (SSIM) values and the signal to noise ratio (SNR) values for the reconstructed slices compared to the reference image. These reported values confirm the visually restored slices and show that our model provides a less noisy reconstruction that is closer to the reference image.

Table 1: Synthetic data : SNR and SSIM values for the reconstructed images.

| | SNR (dB) | SSIM |
|---|---|---|
| SENSE method | 18.83 | 0.79 |
| Proposed model | **27.05** | **0.94** |
| Bayesian $\ell_2$ regularization | 25.84 | 0.93 |
| Tikhonov regularization | 20.66 | 0.89 |

The MMSE values of the estimated posteriors of $\hat{\sigma_n^2}$ , $\hat{\omega}$ and $\hat{\lambda}$ are equal to the values 4.69, 0.12 and 41.01, respectively. As regards the noise variance $\hat{\sigma_n^2}$, we notice that the estimate is close to the reference value $\sigma_n^2 = 4$. For the Bernoulli hyperparameter $\hat{\omega}$, the value found indicates a high sparsity level of the target image $\hat{\boldsymbol{\rho}}$.

## 5.2 Experiments with Real data

### *5.2.1 Experiment 1*

In this experiment, we concentrate on validating our algorithm on a real dataset. The used data includes $255 \times 255 \times 14 \times 8$ Gradient-Echo (GE) anatomical images where $255 \times 255$ represents the size of the axial brain slice, 14 represents the number of slices and 8 represents the number of used coils. These data were acquired with a 1.5 Tesla GE Healthcare scanner and a spatial resolution of $0.93 \times 0.93 \times 8mm^3$ with two different reduction factors 2 and 4. Fig. 4(b) (resp. Fig. 4(a)) illustrates the restored slices by the proposed sparse Bayesian model (resp. the SENSE method) for $R = 2$ and $R = 4$. The performance of our sparse Bayesian technique was compared with two recent literature methods. Fig. 4(c) illustrates the restored images by the Bayesian $\ell_2$ regularization, and Fig. 4(d) defines the restored images by the Tikhonov regularization, with $R = 2$ and $R = 4$. The artifacts occurring in Fig. 4(a) are very severe especially when $R = 4$. The existing regularization methods are not able to eliminate these too severe artifacts as shown in Fig. 4(c) and Fig. 4(d). In the same sense, these artifacts are too strong to be eliminated using our method too. To better explain the performance of the proposed model, Fig. 5 illustrates the comparison between difference slices for $R = 2$ and $R = 4$. These difference slices were calculated with respect to the SENSE reconstruction in order to asses the artifacts reduction level. Both the visual inspection of the reconstructed and difference images show that our model better attenuates reconstruction artifacts. This is mainly clear through the difference images where the information is more structural especially next to the main reconstruction artifacts of the SENSE image. For the sake of quantitative evaluation of the artifacts attenuation, Tab. 2 indicates the energy values for the difference images. The reported energy values indicate that the proposed method gives a more significant difference with respect to the SENSE reconstruction, and this in comparison to the Bayesian $\ell_2$ and the Tikhonov regularizations. As regards sparsity, Tab. 3 indicates the $\ell_0$

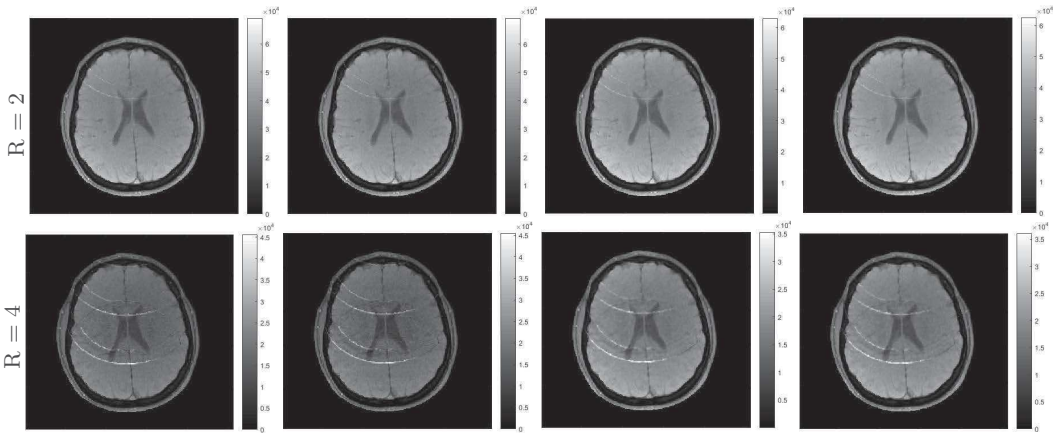


(a) (b) (c) (d)

Fig. 4: Reconstructed pMRI brain images by : (a) the SENSE method, (b) the proposed sparse model , (c) the Bayesian $\ell_2$ regularization, and (d) the Tikhonov regularization, with R = 2 and R = 4.

pseudo-norm ($\|.\|_0$) of the reconstructed images using the competing methods. The reported values indicate a clear advantage for the proposed method in providing sparse image.

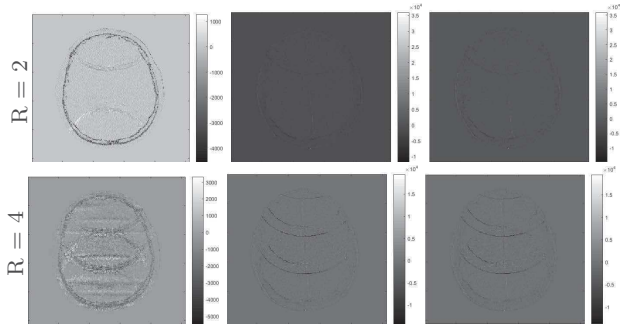


(a) (b) (c)

Fig. 5: Difference images between SENSE and (a) the proposed model, (b) the Bayesian $\ell_2$ regularization, (c) the Tikhonov regularization, for R = 2 and R = 4.

Table 2: Real data : Energy values for the difference images.

| | R = 2 | R = 4 |
|---|---|---|
| Prop. model - SENSE | $\mathbf{1.48e^{+10}}$ | $\mathbf{4.26e^{+10}}$ |
| Bay. $\ell_2$ reg. - SENSE | $8.63e^{+09}$ | $3.35e^{+10}$ |
| Tikhonov - SENSE | $1.28e^{+10}$ | $2.92e^{+10}$ |

Table 3: Real data : sparsity level for the reconstructed Slices.

| | R = 2 | R = 4 |
|---|---|---|
| SENSE | 29080 | 29082 |
| Prop. model | **26954** | **26954** |
| Bay. $\ell_2$ reg. | 29081 | 29081 |
| Tikhonov | 29857 | 29857 |

*5.2.2 Experiment 2*

In this experiment, the proposed Bayesian technique has been validated on a second real data acquired at 3 Tesla Siemens scanner with $R = 2$. Figs. 6(a) and 6(b) illustrate the restored images by the SENSE method and our sparse model, respectively. For comparison, Fig. 6(c) illustrates the restored slice using the Bayesian $\ell_2$ regularization, while Fig. 6(d) illustrates the reconstructed slice by the Tikhonov regularization. Visually, no clear difference in notable between the different methods. However, and to better investigate the performance of our technique, Fig. 7 illustrates the difference images between SENSE and the proposed model, Bayesian $\ell_2$ and Tikhonov regularizations. The energy values of these difference images are equal to $\mathbf{6.80e^{+15}}$, $6.07e^{+15}$ and $6.00e^{+15}$, respectively. For validation purpose, the sparsity level $\|.\|_0$ for the restored images by the proposed model, the SENSE method, the Bayesian $\ell_2$ regularization and the Tikhonov regularization, is equal to **21126**, 22292, 38400 and 38400, respectively. Based on the evaluation of the difference energy and sparsity criteria, the same conclusions as for the first experiment hold, which confirms that our method outperforms SENSE, the Bayesian $\ell_2$ and the Tikhonov regularizations.

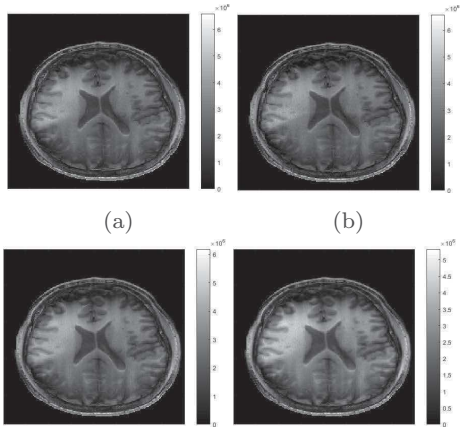

(a) (b)

(c) (d)

Fig. 6: Restored image by : (a) the SENSE method, (b) the proposed sparse model, (c) the Bayesian $\ell_2$ regularization, and (d) the Tikhonov regularization.

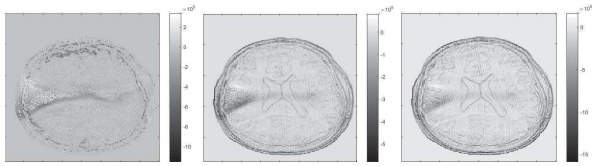

(a) (b) (c)

Fig. 7: Difference images between SENSE and (a) the proposed model, (b) the Bayesian $\ell_2$, (c) the Tikhonov regularizations.

## 6 Conclusion

This paper proposed a novel Bayesian regularization technique for sparse pMRI reconstruction with a BL mixture priors to handle complex-valued pMRI data and promotes two sparsity levels of the target image directly in the spatial domain. The designed method is fully automatic and allows estimating all the regularization methods along with the target image, and this directly from the data. This avoids using a reference scan to do it as usually done for most of the variational regularization methods. The proposed sparse Bayesian model has been validated on a synthetic and real datasets under severe experimental conditions. The achieved results confirm the validity of the proposed sparse Bayesian model. Besides, it outperforms those of recent competing methods of the literature. Our future work will focus on integrating into our model the estimation of the complex-valued sensitivity profiles. It will also consider integrating wavelet transforms in the regularization process.

## References


1. K. Pruessmann, M. Weiger, M. Scheidegger, P. Boesiger, SENSE: sensitivity encoding for fast MRI, Magnetic Resonance in Medicine **42**, 952 (1999)
2. E.J. Candes, J. Romberg, T. Tao, Robust uncertainty principles: exact signal reconstruction from highly incomplete frequency information, IEEE Transactions on Information Theory **52**(2), 489 (2006)
3. M. Griswold, P. Jakob, R. Heidemann, M. Nittka, V. Jellus, J. Wang, B. Kiefer, A. Haase, Generalized autocalibrating partially parallel acquisitions (GRAPPA), Magnetic Resonance in Medicine **47**, 1202 (2002)
4. W. Kyriakos, L. Panych, D. Kacher, C. Westin, C. Bao, R. Mulkern, F. Jolesz, Sensitivity profiles from an array of coils for encoding and reconstruction in parallel (SPACE RIP), Magnetic Resonance in Medicine **44**, 301 (2000)
5. M. Blaimer, F. Breuer, M. Mueller, R. Heidemann, M. Griswold, P. Jakob, SMASH, SENSE, PILS, GRAPPA : how to choose the optimal method, Topics in magnetic resonance imaging (TMRI) **15**, 223 (2004)
6. M. Lustig, D. Donoho, J. Pauly, Sparse MRI: The application of compressed sensing for rapid MR Imaging, Magnetic Resonance in Medicine **58**(6), 1182 (2007)
7. P.H. Kulkarni, S.N. Merchant, S.P. Awate, Bayesian reconstruction of r-fmri from K-T undersampled data using a robust, subject-invariant, spatially-regularized dictionary prior pp. 302–306 (2018)
8. S. Ravishankar, B.E. Moore, R.R. Nadakuditi, J.A. Fessler, Low-rank and adaptive sparse signal (LASSI) models for highly accelerated dynamic imaging, IEEE Transactions on Medical Imaging **36**, 1116 (2017)
9. J. Caballero, D. Rueckert, J.V. Hajnal, Dictionary learning and time sparsity for dynamic MR data reconstruction, IEEE Transactions on Medical Imaging **33**, 979 (2014)
10. S.P. Awate, E.V.R. DiBella, Compressed sensing HARDI via rotation-invariant concise dictionaries, flexible k-space undersampling, and multiscale spatial regularity pp. 9–12 (2013)
11. S.P. Awate, E.V.R. DiBella, Spatiotemporal dictionary learning for undersampled dynamic MRI reconstruction via joint frame-based and dictionary-based sparsity, 9th IEEE International Symposium on Biomedical Imaging (ISBI) pp. 318–321 (2012)
12. J. Hadamard, Sur les problèmes aux dérivées partielles et leur signification physique, Princeton university bulletin **13**, 49 (1902)
13. L. Chaari, J.C. Pesquet, A. Benazza-Benyahia, P. Ciuciu, Autocalibrated regularized parallel MRI reconstruction in the wavelet domain, IEEE International Symposium on Biomedical Imaging pp. 756–759 (2008)
14. L. Ying, D. Xu, Z.P. Liang, On Tikhonov Regularization for image reconstruction in parallel MRI, IEEE Engineering in Medicine and Biology Society **2**, 1056 (2004)
15. B. Liu, L. Ying, M. Steckner, X. Jun, J. Sheng, Regularized SENSE reconstruction using iteratively refined total variation method, IEEE International Symposium on Biomedical Imaging (ISBI) pp. 121–124 (2007)
16. L. Chaari, P. Ciuciu, S. Mériaux, J.C. Pesquet, Spatio-temporal wavelet regularization for parallel MRI reconstruction: application to functional MRI, Magnetic Resonance Materials in Physics, Biology and Medicine **27**(6), 509 (2014)
17. L. Chaari, J.C. Pesquet, A. Benazza-Benyahia, P. Ciuciu, A wavelet-based regularized reconstruction algorithm for SENSE parallel MRI with applications to neuroimaging, Medical Image Analysis **15**, 185 (2011)
18. S. Chaabene, L. Chaari, Bayesian myopic parallel MRI reconstruction, 8th International Symposium on Signal, Image, Video and Communications (ISIVC) **52**, 103 (2016)
19. L. Chaari, Bayesian sparse regularized reconstruction in parallel MRI with sensitivity matrix imprecision, International Conference on Advances in Biomedical Engineering (ICABME) pp. 209–212 (2015)
20. N. Dobigeon, A.O. Hero, J.Y. Tourneret, Hierarchical Bayesian sparse image reconstruction with application to MRFM, IEEE Transactions on Image Processing **18**(9), 2059 (2009)
21. L. Chaari, J. Tourneret, H. Batatia, Sparse Bayesian regularization using Bernoulli-Laplacian priors, 21st European Signal Processing Conference (EUSIPCO) pp. 1–5 (2013)
22. L. Chaari, H. Batatia, J. Tourneret, Sparse Bayesian image restoration with linear operator uncertainties with application to EEG signal recovery, Middle East Conference on Biomedical Engineering (MECBME) pp. 139–142 (2014)
23. F. Costa, H. Batatia, L. Chaari, J. Tourneret, Sparse EEG source localization using Bernoulli Laplacian priors, IEEE Transactions on Biomedical Engineering **62**(12), 2888 (2015)
24. F. Costa, H. Batatia, T. Oberlin, J.Y. Tourneret, EEG source localization based on a structured sparsity prior and a partially collapsed Gibbs sampler, IEEE 6th International Workshop on Computational Advances in Multi-Sensor Adaptive Processing (CAMSAP) pp. 261–264 (2015)
25. F. Costa, H. Batatia, T. Oberlin, C. D'Giano, J.Y. Tourneret, Bayesian EEG source localization using a structured sparsity prior, NeuroImage **144**, 142 (2017)
26. L. Chaari, J.Y. Toumeret, C. Chaux, Sparse signal recovery using a Bernoulli generalized Gaussian prior, 23rd European Signal Processing Conference (EUSIPCO) pp. 1711–1715 (2015)
27. L. Chaari, H. Batatia, N. Dobigeon, J. Tourneret, A hierarchical sparsity-smoothness Bayesian model for $\ell_0 + \ell_1 + \ell_2$ regularization, IEEE International Conference on Acoustics, Speech and Signal Processing (ICASSP) pp. 1901–1905 (2014)
28. M. Guerquin-Kern, D.V.D. Ville, C. Vonesch, J.C. Baritaux, K.P. Pruessmann, M. Unser, Wavelet regularized reconstruction for rapid MRI, IEEE International Symposium on Biomedical Imaging (ISBI) pp. 193–196 (2009)
29. C. Robert, G. Castella, Monte Carlo statistical methods, Springer, New York (2004)
30. S. Chaabene, L. Chaari, A. Kallel, Sparse Bayesian pMRI reconstruction with complex Bernoulli-Laplace mixture priors, IEEE 4th Middle East Conference on Biomedical Engineering (MECBME) pp. 193–197 (2018)
31. A. Gelman, D.B. Rubin, Inference from iterative simulation using multiple sequences, Statistical science **7**(4), 457 (1992)
32. A. Tikhonov, Tikhonov Regularization of incorrectly posed problems, Soviet Mathematics Doklady **4**, 1624 (1963)
33. Z. Wang, A.C. Bovik, H.R. Sheikh, E.P. Simoncelli, Image quality assessment: From error visibility to structural similarity, IEEE Transactions on Image Processing **13**(4), 600 (2004)